Journal Name

ARTICLE

High thermoelectric performance of Higher Manganese Silicides prepared by Ultra-fast Thermal Explosion

Xiaoyu She,[a] Xianli Su,[*a] Huizhen Du,[a] Tao Liang,[a] Gang Zheng,[a] Yonggao Yan,[a] Rizwan Akram,[a] Ctirad Uher,[b] Xinfeng Tang[*a]

Higher manganese silicide (HMS) is an environment-friendly p-type thermoelectric material with attractive performance and high stability in the intermediate temperature range (500 K-800 K). Due to the high melting point of HMS, the preparation methods reported previously always contain energy-intensive processes requiring long preparation periods and high cost. In this study, thermal explosion (TE) was adopted for a facile preparation of high performance HMS via a low cost route. During a typical thermal explosion (TE) process, nanostructured polycrystalline single-phase HMS powder with excellent thermoelectric performance is obtained in an ultra-short period of time (about 10 min). Dense bulk samples are then prepared by a rapid plasma activated sintering (PAS) technique. With Ge substituted in Si sites, significant increase can be observed, which further enhanced the electrical properties. Results show that the Ge doped sample $Mn(Ge_{0.015}Si_{0.985})_{1.75}$ prepared via the TE-PAS technique exhibits a maximum ZT of 0.62 at 840 K, which demonstrates that the TE-PAS technique is a versatile route for rapid fabrication of HMS and other thermoelectric materials.

Introduction

Thermoelectric conversion technology[1] can achieve a direct conversion between heat and electricity through the Seebeck effect (power generation) and the Peltier effect (thermoelectric cooling). It is considered an environmentally friendly energy conversion technology with no reliance on moving parts, free of noise, and exceptionally reliable. Therefore, it has attracted great attention world-wide especially for applications in the area of waste-heat-recovery. The thermoelectric performance is gauged by the figure of merit $ZT = T\alpha^2\sigma/\kappa$, where s is the electrical conductivity, α is the Seebeck coefficient, κ is the total thermal conductivity, and T is the absolute temperature. An ideal thermoelectric material should behave like "Phonon-Glass , Electron-Crystal"[2-5] having simultaneously high σ, high α, and low κ. Metallic silicides, such as $Mg_2Si^{[6-9, 34]}$, $MnSi_{1.75}(HMS)^{[10-15]}$, have drawn a worldwide attention because of their low-cost, high abundance in the earth's crust, and their non-toxic nature.

Higher manganese silicides have been considered promising thermoelectric materials because of their excellent thermoelectric performance in the temperature range between 500 K–800 K and an outstanding thermal as well as chemical stability. Moreover, with appropriate doping, such as when substituting some Si with Ge, the performance of

HMS can be considerably improved and the ZT reaches about 0.6 at 800 K, making HMS one of the best performing p-type silicide-based thermoelectric material. Traditional synthesis techniques of HMS which rely on arc melting, induction melting, solid state reactions, or mechanical alloying are always time and energy demanding. In addition, $MnSi^{[14, 16-18]}$ often contains metallic impurity phases which have an adverse effect on thermoelectric properties. Such impurity phases are virtually unavoidable because the peritectic reaction between MnSi and Si is rarely brought to a completion. All factors above limit large-scale applications of HMS.

Recently, Su et al.[19-22] developed the self-propagating high-temperature synthesis (SHS) to fabricate thermoelectric materials including Cu_2Se, $CoSb_3^{[20]}$, $Bi_2Te_3^{[22]}$ and other structures which dramatically reduced the time of synthesis down to a few seconds. Moreover, the SHS synthesis is easily scalable without relying on any complex apparatus and consumes little energy. Combustion synthesis can be divided into SHS and Thermal explosion according to the ignition method. For SHS, The synthesis is initiated by point-heating of a small part (usually the bottom) of the sample. Once started, a wave of exothermic reaction sweeps through the remaining material. For thermal explosion, the temperature of the whole pellet reaches the ignition temperature at the same time, the reaction of the whole pellet start at the same time. So the initial temperature is different. For SHS, normally the initial temperature is at room temperature. But for thermal explosion, the initial temperature is determined by the environment.

So far, there has been no report in the literature describing HMS prepared by either form of the combustion synthesis. In our previous publication[21], a new thermodynamic criterion was suggested by our group. Only when the adiabatic temperature is high enough to melt the lower melting point component, the combustion wave can be self-propagated. The adiabatic temperature can be calculated by the following formula.

$$\Delta H = \int_{T_0}^{T_{ad}} C_p dT \qquad (1)$$

Here, ΔH is the enthalpy change in the reaction and C_p stands for the molar heat capacity at constant pressure. As a result, T_{ad} is a function of the initial temperature T_0. We have calculate the adiabatic temperature of $MnSi_{1.70}$ compound with the initial temperature at room temperature as 1314 K. The lower melting point component is Mn which the melting point is 1519 K. Thus the combustion synthesis cannot be self-sustained. Indeed we cannot succeed in synthesis of $MnSi_{1.70}$ compounds by SHS with the initial temperature at room temperature. We try to ignite the reaction at the bottom of the pellet of the mixture. But the combustion wave cannot be self-propagated and go through the whole pellet. XRD pattern of bottom part and the top part of the $MnSi_{1.70}$ are shown in Fig. S1 (ESI†). MnSi compound is observed after ignition by the torch indicating the reaction started. However at the top the pellets of the mixture, none of compounds except single elemental Mn, Si is observed indicating that the reaction cannot be self-sustained after ignition. As we know, the T_{ad} is a function of the initial temperature T_0. Thus we choose to synthesize HMS by thermal explosion to increase the adiabatic temperature. Actually we succeed in synthesis of single phase HMS by thermal explosion. In this work, for the first time, we have employed thermal explosion combined with PAS processing to prepare Ge-doped HMS. We obtained a high performance single-phase bulk material in less than an hour and we investigated correlations between the phase transformation, microstructure evolution and thermoelectric properties of the structure. The thermal explosion method combined with PAS processing not only simplifies and shortens the synthesis process but it also results in an excellent single-phase thermoelectric material. Moreover, the synthesis technique paves the way for mass production of HMS and their large-scale industrial applications.

Experimental

Pure elemental Mn (99.9% purity powder), Si (99.99% purity powder), and Ge (99.99% purity powder) were weighed according to the stoichiometry of $Mn(Ge_xSi_{1-x})_{1.75}$ (x = 0.005, 0.01, 0.015, 0.02 and 0.025). Powders were mixed and ground into a fine powder by hand milling, and then loaded into a steel die and cold-pressed to make a pellet. The pellet sealed in the quartz tube at room temperature was directly put into a furnace with the temperature of 1510 K. After holding in the furnace at 1510 K for 10 min, the quartz tube was directly taken out from the furnace and naturally cool down to room

temperature. Thus obtained product was ground into a powder and sintered by PAS under the pressure of 45 MPa at the temperature of 1273 K in vacuum for 5 minutes. The relative density was over 96% as measured by the Archimedes method. The TE powder and PAS bulks were examined by powder x-ray diffractometry (PANalytical: X' Pert PRO, Cu K_α). The morphology and element distribution were determined by back-scattered electron imaging (FESEM, SU8020) and energy dispersive X-ray (EDX) analysis (Bruker), respectively. The electrical conductivity and the Seebeck coefficient were measured simultaneously by a standard four-probe method (ULVAC-RIKO ZEM-3) in He atmosphere. The thermal conductivity was calculated from the measured thermal diffusivity D, specific heat C_p, and density ρ according to the relationship $\kappa = DC_p\rho$. The thermal diffusivity and the specific heat were determined using a laser flash method with NETZSCH: LFA 457 and a power compensation differential scanning calorimeter TA: DSC Q20 in Ar atmosphere, respectively. All measurements were performed in the temperature range from 300 K to 820 K. The low temperature Hall coefficient measurements (10 K–300 K) were performed using a Physical Properties Measurement System (PPMS-9, Quantum Design), with a five-probe sample configuration by sweeping the magnetic field between -1.0 T and 1.0 T. The carrier concentration (n) and the room temperature Hall mobility (μ_H) were obtained from the Hall coefficient (R_H) and the electrical conductivity by the relation：$n=1/e|R_H|$ and $\mu_H=\sigma|R_H|$, respectively, where e is the electron charge.

Results and Discussion

To explore the synthesis process, we collected powder XRD patterns of samples synthesized at different temperatures (973 K, 1073 K, 1173 K, 1273 K, 1373K, 1510 K), as shown in Fig. 1(a). The raw elements did not react at all when the temperature of the TE process was lower than 1073 K. The phase composed of $MnSi_{1.75}$, MnSi and Si was obtained above 1173 K. At still higher temperatures, above 1373 K, a single-phase material was obtained. To gain more insight into the synthesis mechanism, we studied the influence of time on the evolution of the HMS phase at 1510 K. We noticed that three phases, namely MnSi, $MnSi_{1.75}$ and Si, were present within the holding time of 50 seconds, see Fig. 1(b). Furthermore, we found that, as the time went on, the concentration of the $MnSi_{1.75}$ phase increased and MnSi and Si phases gradually disappeared, see Fig. 1(b). To check what happens, we weighted raw elements with the stoichiometry of MnSi and applied the TE process at 1510 K for the same 50 seconds. The pure MnSi phase was synthesized in less than 50 s with no trace of $MnSi_{1.75}$, see Fig. 2(a). Moreover, thus obtained single-phase MnSi was subsequently mixed with the Si powder in the stoichiometric ratio of 1:0.75 and the TE process was applied again at 1510 K for different holding times. As the holding time increased, the concentration of the MnSi phase decreased and MnSi transformed into $MnSi_{1.75}$ completely after 10 min, as shown in Fig. 2(b). All the above results validated the phase transformation process of HMS during the thermal explosion

synthesis which proceeded in two steps: (1) Mn+Si→MnSi; (2)MnSi+0.75Si→MnSi$_{1.75}$.
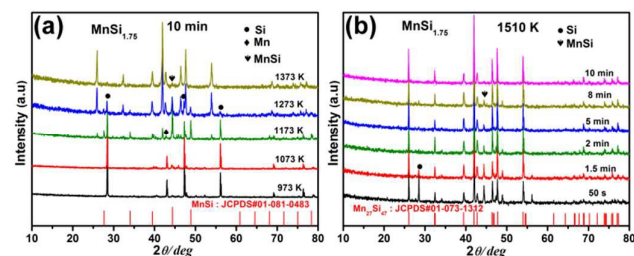
Fig. 1 (a) XRD patterns of MnSi$_{1.75}$ samples synthesized at different temperatures while keeping the time constant at 10min; (b) XRD patterns of MnSi$_{1.75}$ samples synthesized at 1510 K for different times.
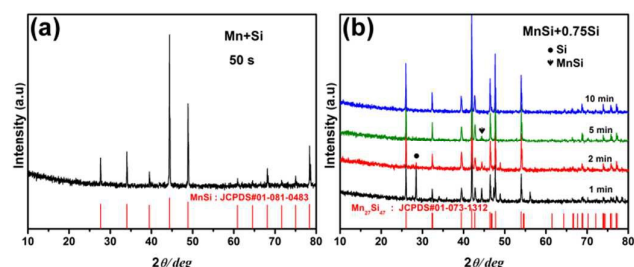
Fig. 2 (a) XRD pattern of a material synthesized by thermal explosion during 50 s starting with pure Mn and Si in the 1:1 ratio; (b) XRD patterns of a material synthesized by thermal explosion for variable times starting with MnSi and pure Si in the 1:0.75 ratio.

Subsequently, we applied the same synthesis process to Ge-doped HMS. The phase composition of compounds with different Ge-doping contents synthesized by the TE-PAS process, Mn(Ge$_x$Si$_{1-x}$)$_{1.75}$ (x = 0.005, 0.01, 0.015, 0.02 and 0.025), was detected by powder XRD and is shown in Fig. 3. Obviously, all samples are single-phase structures, except for the two most heavily doped samples (x = 0.02 and 0.025). The main diffraction patterns closely agree with the JCPDS card 01-073-1312. In the case of the x = 0.02 and x = 0.025 samples, the doping level apparently exceeded the solubility limit of Ge in the HMS compound. This resulted in segregated Ge, the excess of Si in the structure, and the consequent appearance of the MnSi secondary phase. However, due to a very low doping concentration, no Ge impurity phase was actually detected by x-rays. The lattice parameters (*a* and *c*) calculated by the Rietveld method by the Full Profile analysis are shown in Fig. 3(b). No change was observed on the ab lattice plane, but the lattice parameter *c* increased monotonously as the concentration of Ge increased before reaching a constant value at about x = 0.02, indicating that Ge substituting at Si sites has the solubility limit of about 2.0 at%.
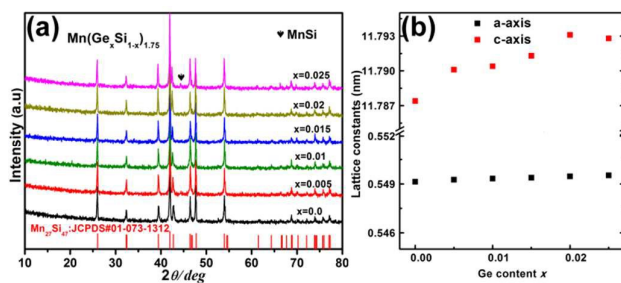
Fig. 3 (a) XRD patterns of TE-PAS Mn(Ge$_x$Si$_{1-x}$)$_{1.75}$ samples; (b) The lattice parameters (*a* and *c*) of TE-PAS Mn(Ge$_x$Si$_{1-x}$)$_{1.75}$ samples calculated by the Rietveld method.

Microstructural morphologies of the undoped sample are shown in Figs. 4(a)-(d). Fig. 4(a) shows secondary-electron images of the mixed powder of raw elements, Fig. 4(b) is the image of a powder after the thermal explosion, and Figs. 4(c) and 4(d) are images of fracture surfaces of the TE-PAS bulk. Raw element powders with the average grain size of about 1 μm-10 μm transformed after thermal explosion to a material with 5 μm-20 μm grains. These grains were covered by ~200 nm *in-situ*-formed grains. After the PAS sintering, FESEM images displayed a highly compacted material in good agreement with the density measurements. The average grain size of the final product was about 10 μm, and there were many 100-200 nm nanoparticles distributed homogeneously on the grains. The particular microstructure may affect thermoelectric properties, especially thermal characteristics. Interestingly, there is no observable secondary phase by the EDS analysis that would correspond to the XRD results. Figs. 4(e) and 4(f) show back scattering electron images (BSEI) of carefully polished surfaces of Mn(Ge$_{0.015}$Si$_{0.985}$)$_{1.75}$ and Mn(Ge$_{0.02}$Si$_{0.98}$)$_{1.75}$, respectively. The elemental distribution maps of Mn(Ge$_{0.015}$Si$_{0.985}$)$_{1.75}$ indicate that all three constituents are evenly distributed on the microscale with no serious agglomeration. The elements in HMS compounds are distributed homogeneously for samples with x≤0.015, indicating that the TE-PAS process, indeed, yields a highly homogeneous HMS compound. Ge-rich areas are clearly observed in the Mn(Ge$_{0.02}$Si$_{0.98}$)$_{1.75}$ sample, indicating the solubility limit of Ge was exceeded at x=0.02. The real solubility limit of Ge of less than 2 at% matches well that of 1.8 at% in a single-crystal reported by Nikitin et.al.[23] and 1.6 at% reported by Zhou et.al.[11]
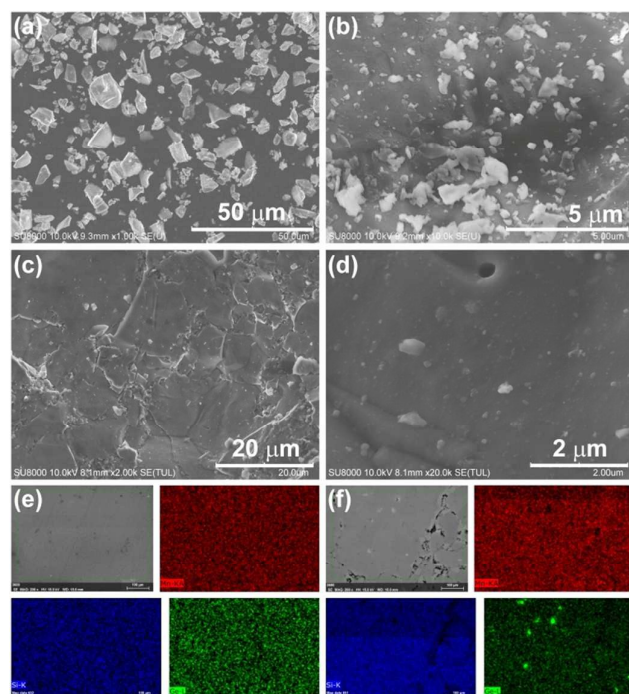
Fig. 4 (a)-(b) FESEM for the MnSi$_{1.75}$ powder before PAS; (c)-(d) FESEM for the MnSi$_{1.75}$ bulk after PAS; (e) Elemental distribution in the Mn(Ge$_{0.015}$Si$_{0.985}$)$_{1.75}$ sample; (f) Elemental distribution in the Mn(Ge$_{0.02}$Si$_{0.98}$)$_{1.75}$ sample.

Temperature dependence of the electrical conductivity for samples with different Ge-content is shown in Fig. 5(a). The electrical conductivity decreases monotonously with the increasing temperature, indicating a degenerate transport behavior. The undoped sample shows an increasing trend in the electrical conductivity at 850 K, suggesting a contribution from intrinsic excitations. The electrical conductivity gradually increases with the increasing Ge-content.

Tab. 1 Hall coefficient R_H, carrier concentration n, Hall mobility μ_H, effective mass m^*, and Lorenz number L for Mn(Ge$_x$Si$_{1-x}$)$_{1.75}$ samples at 300 K.

Samples	R_H (10^{-9}m^3/C)	n (10^{21}cm^{-3})	μ_H (cm^{2}V^{-1}s^{-1})	m^*/m_0	L (10^{-8}V^{2}K^{-2})
x=0.0	3.51	1.78	2.14	9.16	1.83
x=0.005	2.40	2.60	1.63	12.02	1.83
x=0.01	2.52	2.48	1.75	12.06	1.81
x=0.015	2.44	2.56	1.86	12.14	1.82
x=0.02	1.92	3.26	1.50	13.55	1.84

To better understand electronic properties, we measured the Hall coefficient at low temperatures (10 K-300 K), as shown in Fig. 6. and Table 1. The Hall coefficient of all samples is positive, indicating p-type semiconductors. The carrier concentration exhibits a plateau at low temperatures characteristic of heavily doped semiconductors and it increases as the Ge-content increases. Ge is an iso-electronic dopant and, as such, should not affect the carrier density. However, the covalent radius of Ge is larger than that of Si (r_{Ge}=1.22 Å, r_{Si}=1.10 Å) and causes a substantial lattice

distortion which alters the bonding strength and leads to a notable increase in the concentration of holes. The carrier mobility calculated from the Hall coefficient and the electrical conductivity is shown in Fig. 6(b). With the increasing content of Ge, the carrier scattering intensifies. Below 300 K, the temperature dependence changes from the T$^{-3/2}$ power law behavior (acoustic-phonon scattering) of the undoped sample to a weaker temperature dependence as the content of Ge increases. Overall, the higher carrier concentration upon doping leads to an increased electrical conductivity.
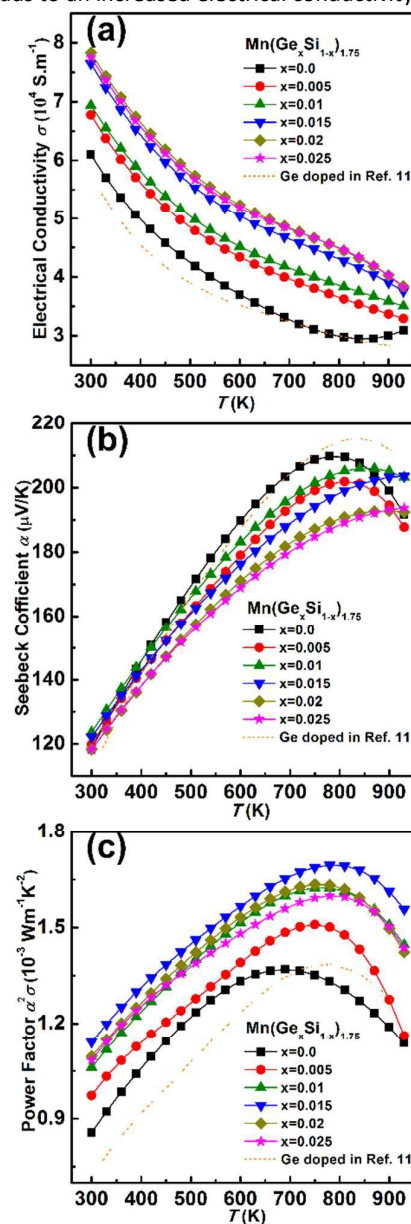
Fig. 5 (a) The temperature dependent electrical conductivity for samples with different Ge-content; (b) The temperature dependence of the Seebeck coefficient; (c) The temperature dependence of power factor *PF*.
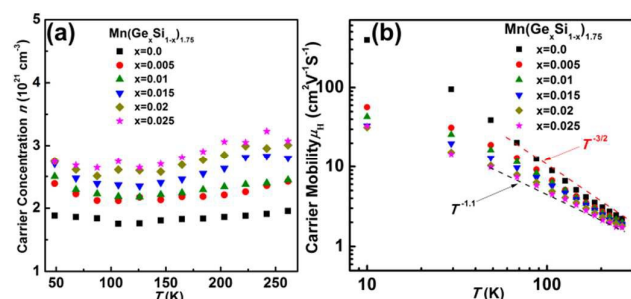
Fig. 6 (a) The temperature dependence of the carrier concentration between 10 K and 300 K; (b) The temperature dependence of carrier mobility at 10 K-300 K.

Fig. 5(b) displays the temperature dependence of the Seebeck coefficient α. Positive values of α are in accord with the Hall coefficient. The Seebeck coefficient increases with the increasing temperature and, as far as its magnitude is concerned, shows an opposite trend with the electrical conductivity upon Ge doping. Samples with the low content of Ge (x≤0.01) show a distinct turn-over in their temperature dependence of α near 800 K, symptomatic of the onset of intrinsic excitations. From the temperature where the Seebeck coefficient achieves its maximum value one can evaluate an approximate size of the band gap using the formula $E_g = 2e\alpha_{max}T_{max}$[24].Thus obtained band gaps are about 0.33-0.35 eV and substantially independent of Ge doping. On the basis of the Boltzmann transport equation and assuming a simplified single parabolic band model with the carrier scattering dominated by acoustic phonons, the Seebeck coefficient and the carrier concentration can be expressed via Eqs. 2-5 as[7, 25-27]

$$\alpha = \pm\frac{k_B}{e}\left[\eta_F - \frac{\left(r+\frac{5}{2}\right)F_{r+\frac{3}{2}}(\eta_F)}{\left(r+\frac{3}{2}\right)F_{r+\frac{1}{2}}(\eta_F)}\right] \quad (2)$$

$$F_i(\eta_F) = \int_0^\infty \frac{x^i dx}{1+\exp(x-\eta_F)} \quad (3)$$

$$\eta_F = E_F/(k_B T) \quad (4)$$

$$n = \frac{4\pi(2k_B Tm^*)^{\frac{3}{2}}}{h^3}F_{\frac{1}{2}}(\eta_F) \quad (5)$$

Here, $F_i(\eta_F)$ is the Fermi integral, η_F is the reduced Fermi level, k_B is the Boltzmann constant, m^* is the effective mass, h is the Planck constant, r is the scattering factor, here $r = -1/2$, and T is the absolute temperature. The calculated m^* of the undoped sample is 9.16 m_0, close to the result reported previously[10, 12]. This rather high value of the effective mass undoubtedly reflects on a very flat valence band[28].

To confirm the increase in the DOS effective mass by Ge-doping, low temperature (2-20 K) heat capacity C_p was measured for both the undoped MnSi$_{1.75}$ and Ge-doped Mn(Ge$_{0.015}$Si$_{0.985}$)$_{1.75}$ samples. Low temperature heat capacity C_p of solids can be described by Eqs. 6 and 7 as[7, 9, 29]

$$C_p = \gamma T + bT^3 \quad (6)$$

$$\gamma = \frac{\pi^2}{3}k_B^2 N(E_F) = 1.36\times10^{-4}\times V_{mol}^{2/3}n_\gamma^{1/3}\frac{m^*}{m_0} \quad (7)$$

Here, γT is the carrier contribution and bT^3 is the lattice contribution. γ is the Sommerfeld coefficient given in Eq. 7 where $N(E_f)$ is related to the electronic DOS at the Fermi level. V_{mol}, n_γ, m^* and m_0 in Eq. 7 stand for the molar volume, the number of carriers per formula unit, the DOS effective mass, and the mass of a free electron in vacuum, respectively. Fig. 7 shows C_p/T as a function of T^2 for the undoped sample and the sample with x=0.015, respectively. From the intercept on the C_p/T axis one obtains the value of γ. As Fig. 7 indicates, the value of γ of the Ge-doped sample Mn(Ge$_{0.015}$Si$_{0.985}$)$_{1.75}$ is significantly higher than the value of γ for the undoped sample, in good agreement with the increase in the effective mass m^*.
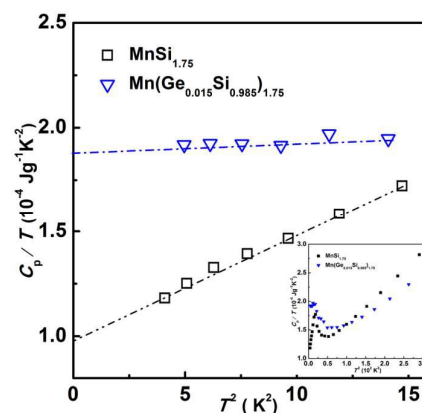
Fig. 7 The relationship between C_p and T in the 2 K -20 K range.

The relationship between the Seebeck coefficient α and the carrier concentration n_H, often known as the Pisarenko plot, is expressed through Eq. 8 and is illustrated in Fig. 8 together with some previously obtained data on doped HMS.

$$\alpha = \frac{8\pi^2 k_B^2 T}{3eh^2}m^*\left(\frac{\pi}{3n}\right)^{\frac{2}{3}} \quad (8)$$
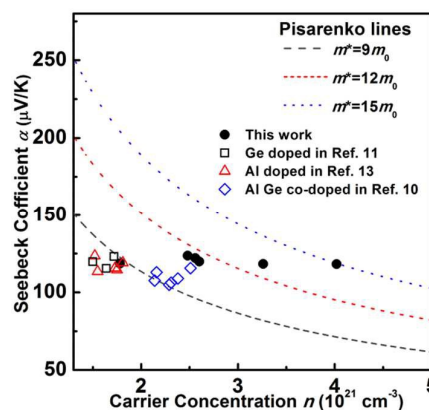
Fig. 8. Relationships between the Seebeck coefficient α and the carrier concentration n_H and the Pisarenko plots based on the SPB model.

Compared to other doping elements reported before, the enhanced effective mass upon Ge doping is responsible for somewhat elevated values of the Seebeck coefficient we observe at the same level of doping. The fits in Fig. 5 suggest that the effective mass of our samples progressively increases with the content of Ge and covers the range between $9m_0$-$15m_0$. We note that this dependence of the effective mass on the content of Ge is opposite to what was reported previously for Re-doped HMS[12].

Temperature dependence of the power factor PF is shown in Fig. 5(c). The highest PF is about 1.7 mWm^{-1}K^{-2} obtained with the 1.5at% Ge-doped sample at close to 800 K, the value some 30% higher than the power factor of the undoped sample and also much higher than the best performing Ge-doped sample (dashed line) in Ref. 11[11].

Figs. 9(a) and 9(b) display the temperature dependence of the thermal conductivity κ and the lattice thermal conductivity κ_L. The thermal conductivity initially decreases with the increasing temperature and, above about 650 K, turns up and rapidly increases due to the onset of intrinsic excitations. The trend is similar for the Ge-doped samples except that their thermal conductivity is somewhat lower. The lowest thermal conductivity of about 2.1 Wm^{-1}K^{-1} at 660 K is obtained with the 1at% Ge-doped sample. Again, assuming a single parabolic band model dominated by acoustic phonon scattering, the Lorenz number L can be obtained from Eqs. 9 and 10 and is approximately 1.6×10^{-8} V^{2}K^{-2}, well in the range of values reported in Ref. 12[12]. The lattice thermal conductivity contribution can be derived using the Wiedemann–Franz law $\kappa_L=\kappa-\kappa_e=\kappa-L\sigma T$,[25] as shown in Fig. 9(b). The lattice thermal conductivity decreases monotonously with the increasing concentration of Ge. The lowest lattice thermal conductivity is obtained in the sample doped with 2at% of Ge, indicating that Ge contributes to the lattice distortion and enhances point defect scattering.

$$L = \left(\frac{k_B}{e}\right)^2 \left[\frac{\left(r+\frac{7}{2}\right)F_{r+\frac{5}{2}}(\eta_F)}{\left(r+\frac{3}{2}\right)F_{r+\frac{1}{2}}(\eta_F)} - \delta^2(\eta_F)\right] \qquad (9)$$

$$\delta(\eta_F) = \frac{\left(r+\frac{5}{2}\right)F_{r+\frac{3}{2}}(\eta_F)}{\left(r+\frac{3}{2}\right)F_{r+\frac{1}{2}}(\eta_F)} \qquad (10)$$
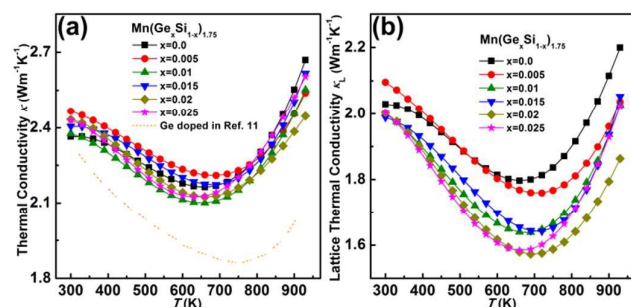
Fig. 9 (a) The temperature dependence of the thermal conductivity κ; (b) The temperature dependence of the lattice thermal conductivity κ_L.

The decreasing trend of the lattice thermal conductivity between 300 K-650 K is attributed to the decreased mean-free path of phonons caused by Umklapp phonon processes. The rising lattice thermal conductivity at high temperatures is due to the bipolar

effect. Because Ge-doping increases the carrier density, the onset of intrinsic excitations is shifted to slightly higher temperatures. Here we use the formula of Kitagawa[30] to evaluate the contribution of the bipolar term κ_{Bi} to the overall thermal conductivity. When the temperature is higher than the Debye temperature θ_D, the lattice thermal conductivity of all samples seems to be limited by Umklapp phonon processes that lead to the 1/T dependence of κ_L. Thus, the real lattice thermal conductivity above θ_D can be estimated as shown in Fig. 10 (dashed lines). It seems that a slight amount of Ge restrains the bipolar effect as κ_{Bi} of the undoped sample is about 0.54 Wm^{-1}K^{-1} while the value for the 0.5at% Ge-doped sample is only about 0.37 Wm^{-1}K^{-1}. The minimum lattice thermal conductivity κ_{min} can be evaluated based on the model of Cahill[31-33] from Eqs. 11 and 12 as

$$\kappa_{min} = \left(\frac{\pi}{6}\right)^{1/3} k_B n_a^{2/3} \sum_i v_i \left(\frac{T}{\theta_i}\right)^2 \int_0^{\theta_i/T} \frac{x^3 e^x}{\left(e^x-1\right)^2} dx \qquad (11)$$

$$\theta_i = v_i \left(\hbar/k_B\right)\left(6\pi^2 n_a\right)^{1/3} \qquad (12)$$

Here the summation is over the three polarization modes, κ_B is the Boltzmann constant, n_a is the number density of atoms, $\hbar$ is the reduced Planck constant, and v_i is the sound velocity for each polarization mode. According to the result of Chen et al.[12], the shear and transverse sound velocities of the HMS compound are 4.62×10^5 cm·s^{-1} and 7.55×10^5 cm·s^{-1}, respectively. The κ_{min} result is shown in Fig. 9 (dotted line). The actual κ_L of the undoped sample is fairly close to κ_{min} at 700 K and would likely continue to be so if not for the bipolar effect dominating the high temperature behavior. Ge-doped samples, on account of stronger point defect scattering, come even closer to the minimum thermal conductivity.
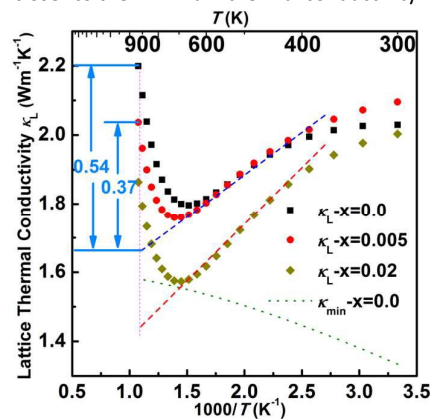
Fig. 10. The T^{-1} dependence of the lattice thermal conductivity and the bipolar thermal conductivity.

Fig. 11 presents the dimensionless thermoelectric figure of merit ZT as a function of temperature. The highest ZT is obtained with the 1.5at% Ge-doped sample and reaches its maximum value of 0.62 at 840 K, some 30% higher value that for the undoped sample. This value is essentially identical to the Ge-doped HMS sample prepared by induction melting followed by hot-press sintering[11]. Thus, we have achieved equally good thermoelectric properties with Ge-doped HMS accept that our synthesis procedure is much less

demanding of the energy and shortens the synthesis time to less than an hour.
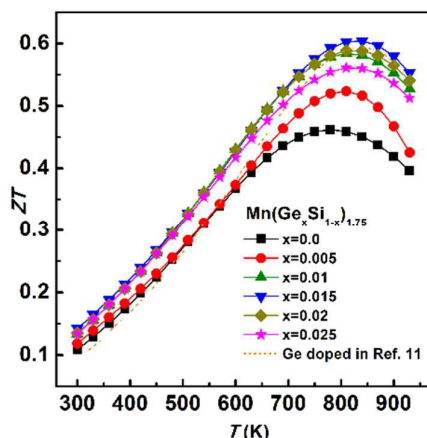
Figure 11. The temperature dependence of the figure of merit *ZT*.

Conclusions

We have prepared Ge-doped HMS compounds using the thermal explosion route followed by plasma activated sintering and obtained a high performance material in a very short period of time and with minimal use of energy. Based on our structural data, the solubility limit of Ge in HMS is no greater than 2%. Ge doping increases the carrier concentration of HMS and decreases the lattice thermal conductivity on account of enhanced point defect scattering. Large Seebeck coefficients in conjunction with increased electrical conductivity lead to large effective masses which increase with the content of Ge and fall within the range of $9m_0$-$15m_0$. The maximum value of the dimensionless figure of merit of 0.62 is achieved at 840 K with the 1.5at% Ge-doped sample, similar to the best *ZT* value reported for HMS. We obtained such a competitive HMS performance using a synthesis which is very rapid and consumes little energy. The technique of TE-PAS is thus suitable for a large scale, economical production of high quality HMS materials and likely can be extended to other prospective thermoelectric materials.

Acknowledgements

References

1 A. F. Ioffe, *Semiconductor thermoelements, and Thermoelectric cooling*, A. F. Ioffe, Ed; London, 1957.
2 G. A. Slack and D. M. Rowe, *CRC handbook of thermoelectrics*, D. M. Rowe, Ed., CRC Press: Boca Raton, FL, USA 1995, 407.
3 G. Min and D. Rowe, *J. Mater. Sci. Lett.,* 1999, **18**, 1305-1306.
4 J. R. Sootsman, D. Y. Chung and M. G. Kanatzidis, *Angew. Chem. Int. Ed.,* 2009, **48**, 8616-39.
5 G. J. Snyder and E. S. Toberer, *Nature Mater.,* 2008, **7**, 105-114.
6 W. Liu, Q. Zhang, X. Tang, H. Li and J. Sharp, *J. Electron. Mater.,* 2011, **40**, 1062-1066.
7 Q. Zhang, L. Cheng, W. Liu, Y. Zheng, X. Su, H. Chi, H. Liu, Y. Yan, X. Tang and C. Uher, *Phys. Chem. Chem. Phys.,* 2014, **16**, 23576-83.
8 W. Liu, X. Tang, H. Li, J. Sharp, X. Zhou and C.Uher, *Chem. Mater.,* 2011, **23**, 5256-5263.
9 W. Liu, X. Tan, K. Yin, H. Liu, X. Tang, J. Shi, Q. Zhang and C. Uher, *Phys. Rev. Lett.,* 2012, **108**, 166601.
10 X. Chen, A. Weathers, D. Salta, L. Zhang, J. Zhou, J. B. Goodenough and L. Shi, *J. Appl. Phys.,* 2013, **114**, 173705.
11 A. J. Zhou, T. J. Zhu, X. B. Zhao, S. H. Yang, T. Dasgupta, C. Stiewe, R. Hassdorf and E. Mueller, *J. Electron. Mater.,* 2009, **39**, 2002-2007.
12 X. Chen, S. N. Girard, F. Meng, E. Lara-Curzio, S. Jin, J. B. Goodenough, J. Zhou and L. Shi, *Adv. Energy Mater.,* 2014, **4**, 140052.
13 W. Luo, H. Li, F. Fu, W. Hao and X. Tang, *J. Electron. Mater.,* 2011, **40**, 1233-1237.
14 W. Luo, H. Li, Y. Yan, Z. Lin, X. Tang, Q. Zhang and C. Uher, *Intermetallics*, 2011, **19**, 404-408.
15 V. Ponnambalam, D. T. Morelli, S. Bhattacharya, T. M. Tritt, *J. Alloy. Compd.,* 2013, **580**, 598-603.
16 A. Gokhale and R. Abbaschian, *Bull. Alloy Phase Diag.,* 1990, 11, 468-480.
17 T. Itoh and M.Yamada, *J. Electron. Mater.,* 2009, **38**, 925-929.
18 L. D. Ivanova, *Inorg. Mater.*, 2011, **47**, 965-970.
19 X. Su, F. Fu, Y. Yan, G. Zheng, T. Liang, Q. Zhang, X. Cheng, D. Yang, H. Chi, X. Tang, Q. Zhang and Uher C. *Nat. Commun.*, 2014, **5**, 4908.
20 T. Liang, X. Su, Y. Yan, G. Zheng, Q. Zhang, H. Chi, X. Tang and C. Uher, *J. Mater. Chem. A*, 2014, **2**, 17914-17918.
21 T. Liang, X. Su, X. Tan, G. Zheng, X. She, Y. Yan, X. Tang and C. Uher, *J. Mater. Chem. C*, 2015, doi: 10.1039/C5TC01573A.
22 G. Zheng, X. Su, T. Liang, Q. Lu, Y. Yan, C. Uher and X. Tang, *J. Mater. Chem. A*, 2015, **3**, 6603-6613.
23 E.N. Nikitin A. F. S., V.I. Tarasov and AI. Zaslavskii, *Akad. Nauk SSSR. Neorg. Mater.*, 1970, **6**, 604-605.
24 H. Goldsmid and J. Sharp, *J. Electron. Mater.,* 1999, **28**, 869-872.
25 G. S. Nolas, J. Sharp and J. Goldsmid, *Thermoelectrics: basic principles and new materials developments*, Springer, New York, 2001.
26 S. Wang, X. She, G. Zheng, F. Fu, H. Li and Tang X., *J. Electron. Mater.,* 2012, **41**, 1091-1099.
27 S. Wang, G.Zheng, T. Luo, X. She, H. Li and X. Tang, *J. Phys. D. Appl. Phys.,* 2011, **44**, 475304.
28 D. Migas, V. Shaposhnikov, A. Filonov, V. Borisenko and N. Dorozhkin, *Phys. Rev. B*, 2008, **77**, 075205.
29 M. Ahrens, R. Merkle, B. Rahmati and J. Maier, *Physica. B. Condensed Matter.*, 2007, **393**, 239-248.
30 H. Kitagawa, M. Wakatsuki, H.Nagaoka, H. Noguchi, Y. Isoda, K. Hasezaki and Y. Noda, *J. Phys. Chem. Solids*, 2005, **66**, 1635-1639.
31 D. G. Cahill, S. K. Watson and R. O. Pohl, *Phys. Rev. B*, 1992, **46**, 6131-6140.
32 W. Xie, J. He, H. J. Kang, X. Tang, S. Zhu, M. Laver, S. Wang, J. R. Copley, C. M. Brown, Q. Zhang and T. M. Tritt, *Nano Lett.*, 2010, **10**, 3283-9.
33 S. Wang, F. Fu, X. She, G. Zheng, H. Li and X. Tang, *Intermetallics*, 2011, **19**, 1823-1830.
34 J. Bahk, Z. Bian, and A. Shakouri, *Phys. Rev. B*, 2014, **89**, 075204.

High thermoelectric performance of Higher Manganese Silicides prepared by Ultra-fast Thermal Explosion

Xiaoyu She,[a] Xianli Su,[*a] Huizhen Du,[a] Tao Liang,[a] Gang Zheng,[a] Yonggao Yan,[a] Rizwan Akram,[a]

Ctirad Uher,[b] Xinfeng Tang,[*a]

High performance Ge doped HMS are synthesized by thermal explosion—a new method which

paves the way for mass production of HMS and their large-scale industrial applications.